The effect of bubble size on lock-exchange density currents through bubble screens

O'Mahoney, Tom S.D.; Oldenziel, Gosse; Van Der Ven, Pepijn

DOI
10.1061/JHEND8.HYENG-13531

Publication date
2024

Document Version
Final published version

Published in
Journal of Hydraulic Engineering

Citation (APA)
O'Mahoney, T. S. D., Oldenziel, G., & Van Der Ven, P. (2024). The effect of bubble size on lock-exchange density currents through bubble screens. *Journal of Hydraulic Engineering*, *150*(3), Article 04024006. https://doi.org/10.1061/JHEND8.HYENG-13531

The Effect of Bubble Size on Lock-Exchange Density Currents through Bubble Screens

Tom S. D. O'Mahoney[1]; Gosse Oldenziel[2]; and Pepijn van der Ven[3]

Abstract: Bubble screens are used at sea locks to mitigate salt intrusion into inland water systems. In this paper the effectiveness of a bubble screen in delaying the mixing of salt and freshwater via lock exchange was studied. Laboratory-scale experiments investigating the flow field and mixing caused by a bubble screen are presented. The tests include both the homogeneous situation of freshwater on both sides of the screen and the inhomogeneous situation where there is an initial density difference across the screen, which leads to a density current after the lock gate is removed or opened. Optical measurement techniques were applied, giving spatially detailed flow velocities and densities. The parameters varied between tests are the airflow discharge and the bubble size. The results show that the bubble size in the screen had a significant effect with a screen with bubbles of 1–2 mm being more effective at generating a surface flow in the homogeneous case but less effective at keeping the fresh and salt sides separated in the inhomogeneous case, when compared with a screen of 4–6 mm bubbles. The point of maximum effectiveness for separating salt and fresh sides was also shown to be dependent on bubble size. **DOI: 10.1061/JHEND8.HYENG-13531.** *© 2024 American Society of Civil Engineers.*

Introduction

Bubble screens are sometimes applied at shipping locks near the sea to mitigate salt intrusion, which occurs as a result of density currents exchanging salt and freshwater in the lock chamber during lock operations. This salt intrusion is often undesirable because the inland water system may be a source of freshwater for industry, agriculture, and drinking water, or the salt intrusion may interfere with the ecology of the hinterland (Kerstma et al. 1994). Many measures are available to mitigate the salt intrusion at locks (van der Kuur 1986). Most require some additional infrastructure such as culvert systems that are integrated into the leveling system of the lock or require the use of freshwater resources for flushing of the lock or waterway. Bubble screens, however, can be retrofitted to an existing lock without changing the existing hydraulic infrastructure and do not require the use of freshwater to be effective. The first application of bubble screens for this purpose was in the Netherlands in the 1960s (Abraham and van der Burgh 1964) and this work is still used as a guideline for the design of bubble screens and the required airflow rates. This study builds on theoretical, model, and field-scale research of bubble screens in water of a single density, which had been proposed as a means of damping waves (Taylor 1955; Evans 1955; Bulson 1961). Bulson (1961) found a relation between the airflow rate of the screen and the generated current at the surface, namely, the velocity at the surface, V_m, as well as the height of the surface current, δ. Other applications of bubble screens also include enhancing mixing in lakes, reservoirs, and wastewater treatment systems (Wen and Torrest 1987; Neto et al. 2008; Lima Neto et al. 2008), as well as possible applications for managing the morphological evolution of bends in rivers (Blanckaert et al. 2008; Dugué et al. 2015) or for reducing salt intrusion in rivers (Nakai and Arita 2002).

Some measurements of vertical currents inside the bubble screen have been made (Bulson 1961; Kobus 1968) and many more are available inside bubble plumes (Wang et al. 2019). However, owing to the difficulty of measuring inside the bubble screen, most measurements have been made in the current generated around the bubble screen. The most commonly measured quantities for a bubble screen in homogeneous water are the velocity generated at the surface, the surface current height, and the size of the recirculation cells generated on either side of the bubble screen (Fig. 1). Bulson (1961) measured the surface velocity at a location away from the screen, at a distance equal to one water depth, in tests ranging from laboratory scale to up to 10-m depth in field scale, and derived the following relation:

$$V_m = 1.46(gq)^{1/3}\left[1 + \frac{D}{H_0}\right]^{1/3} \qquad (1)$$

where g (m/s^2) = gravitational acceleration; q (m^2/s) = airflow rate per unit width; D (m) = water depth; and H_0 (m) = atmospheric pressure in length of the column of water.

The maximum surface velocity occurs closer to the bubble screen as has been shown in many studies (Bulson 1961; Abraham and van der Burgh 1964; Wen and Torrest 1987; Fanneløp et al. 1991). Wall and surface jet theory would suggest a decay in the velocity away from the bubble screen centerline proportional to $x^{-1/2}$. The data of Bulson (1961) and Wen and Torrest (1987) seem to support this, but Abraham and van der Burgh (1964) approximate their data with linear relations. This decay can also be affected by the available distance between the location of the bubble screen and the opposite boundary (Fanneløp et al. 1991), which also can affect the size of the recirculation cells that develop on either side of the screen. These varied between the mentioned studies from two times the depth to seven times the depth. A relation for the nondimensional circulation as a function of the airflow rate is given in Keetels et al. (2011).

---

[1] Researcher and Consultant, Hydraulic Engineering, Deltares, Boussinesqweg 1, Delft 2629 HV, Netherlands (corresponding author). Email: tom.omahoney@deltares.nl

[2] Researcher and Consultant, Hydraulic Engineering, Deltares, Boussinesqweg 1, Delft 2629 HV, Netherlands; Guest Researcher, Laboratory for Aero and Hydrodynamics, Delft Univ. of Technology, P.O. Box 177, Delft 2600 MH, Netherlands. Email: gosse.oldenziel@deltares.nl

[3] Researcher and Consultant, Hydraulic Engineering, Deltares, Boussinesqweg 1, Delft 2629 HV, Netherlands. Email: pepijnvanderven@gmail.com

Note. This manuscript was submitted on October 7, 2022; approved on August 25, 2023; published online on February 15, 2024. Discussion period open until July 15, 2024; separate discussions must be submitted for individual papers. This paper is part of the ***Journal of Hydraulic Engineering***, © ASCE, ISSN 0733-9429.

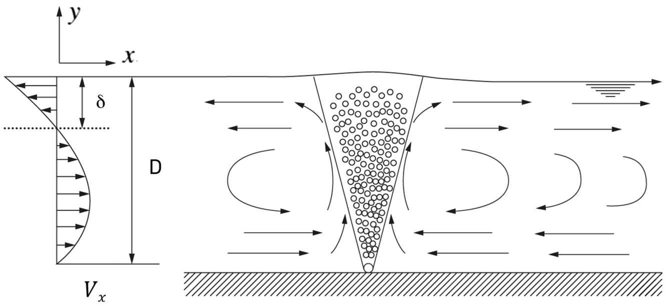

Fig. 1. Definition of flow field elements for a bubble screen in homogeneous water. (#169; 1973 Rijkswaterstaat Communications. Reprinted, with permission, from G. Abraham, P. van der Burgh, and P. de Vos, "Pneumatic barriers to reduce salt intrusions through locks." *Rijkswaterstaat Communications*, The Hague: Government Publishing Office, 17: 67–68.)

The height of the observed surface current, defined as the depth for which the horizontal velocity is directed away from the bubble screen, has also been studied and shown to vary between 20% and 30% of the depth and to grow away from the bubble screen.

The effect of bubble size is largely neglected in these studies of bubble curtains, although this is known to be an important parameter in studies of bubble plumes (Neto et al. 2008), with smaller bubbles leading to larger entrainment and stronger currents, given the same air volume flow rate. This would suggest that bubble screens with smaller bubbles would be more effective at creating the circulation currents of a bubble screen. Bulson (1961), however, claims that the diffuser or sparger size (both orifice size as well as total number of orifices) has little to no effect on the surface currents, although only a limited range of orifice sizes were tested. Similarly, the flow from the bubble screen in a lock is assumed to be two-dimensional (2D) with three-dimensional (3D) effects from the side walls and little dependence on the aspect ratio of the lock chamber or tank (depth/width), although some studies do quantify this (Riess and Fanneløp 1998; Wen and Torrest 1987; Lima Neto et al. 2008). The 3D effects reported in Abraham and van der Burgh (1964) relate to bubble screens that are placed between walls that are not parallel.

When a lock gate separating freshwater from saltwater opens, the lock-exchange phenomenon takes place. This phenomenon has been studied extensively in the laboratory (Benjamin 1968; Rottman and Simpson 1983; Simpson 1997; Shin et al. 2002; Inghilesi et al. 2020; Lombardi et al. 2018; Pérez-Díaz et al. 2018; Nogueira et al. 2018; De Falco et al. 2020). The most recent experimental studies (Marino et al. 2005; Martin and García 2009; Nogueira et al. 2014; Pérez-Díaz et al. 2018; De Falco et al. 2020) use high-resolution optical techniques to capture density fields of the development of the density current, concentrating mostly on the front speed and dynamics but also investigating the interaction with slopes and inclined walls (Dai and Huang 2020; De Falco et al. 2020; Maggi et al. 2023).

For studies of salt intrusion at locks, the salt flux out of the lock is important. Bubble screens as a mitigation measure against salt intrusion at sea locks have mostly been studied at field scale (Abraham et al. 1973; Uittenbogaard and O'Hara 2015; Keetels et al. 2011), with some results at laboratory scale reported (Keetels et al. 2011; Bacot et al. 2022). The field-scale experiments of Delft Hydraulics (Abraham et al. 1973) show that the salt flux out of the lock approximately follows a tanh curve in time, which is nearly linear for the traversal of the density current for the first lock length, L. Here the exchange of saltwater from one side of the gate to the other was measured at field scale with relatively coarse resolution, with and without the bubble screen and for different flow rates. The measurements were made inside the lock and integrated to give a time series of the average density inside the lock chamber volume. A relation was found for the reduction in salt intrusion (relative to a lock exchange without a bubble screen) as a function of supplied airflow rate to the bubble screen and this was used to design bubble screens for practical use at several sea locks in the Netherlands (IJmuiden, Kornwerderzand, Terneuzen). Abraham et al. related the effectiveness of the bubble screen to the nondimensional airflow rate, Froude air number:

$$Fr_a = \frac{(qg)^{1/3}}{(g'D)^{1/2}} \tag{2}$$

It was claimed that flow rates higher than $Fr_a > 1$ would not lead to further reduction in salt intrusion. Field studies (Keetels et al. 2011; Uittenbogaard and O'Hara 2015; Weiler et al. 2015) confirmed that there was a minimum salt transmission factor reached at approximately $Fr_a = 1$. The resolution of these field studies was too coarse to gain much insight in the flow patterns when a bubble screen is combined with a density current. A more recent study (Bacot et al. 2022) made detailed laboratory measurements of the density salt concentration field during a lock exchange with bubble screen for a range of flow rates and found in a minimum salt transmission factor at $Fr_a = 0.93$. For flow rates below $Fr_a = 0.93$, called the breakthrough regime, it was observed that the density flow along the bottom of the tank was still present although attenuated by the bubble screen. A so-called curtain-driven regime was identified for flow rates higher than $Fr_a = 0.93$ whereby the vertical momentum flux of the bubble screen is sufficient to drive all the heavier saltwater to the surface, where it is deflected horizontally outward.

Laboratory-scale experiments of the combination of a bubble screen and a density current in a river-type flow are available (Nakai and Arita 2002). They show that for large enough airflow rates a recirculation cell is created at the fresh side of the bubble screen, which is a mixture of the fresh and saltwater (Fig. 2). This cell is then the source of a new density current in the upstream direction, toward the freshwater side, with a reduced density. The total reduction in salt flux into the freshwater system is therefore a combination of a reduced front speed and reduced salt concentration in the front.

The field studies (Keetels et al. 2011; Uittenbogaard and O'Hara 2015; Weiler et al. 2015) included a comparison of sparger types in order to inform the design of proposed bubble screens at locks in the Netherlands as a salt intrusion mitigation measure. It was claimed that a sparger that produced a more uniform screen of bubbles close to the floor performed better. Keetels et al. (2011) report a screen from their laboratory experiments with bubble sizes ranging between 3 and 5 mm but do not compare the performance with other bubble sizes. Neither the field studies nor the most recent laboratory experiments (Bacot et al. 2022) report the bubble size used.

The current study aims to understand the impact that bubble size can have on the effectiveness of a bubble screen as a separator of salt and freshwater during a lock-exchange flow. It focuses on the regime of operation most used in practice, $Fr_a = 1$, and near the point of maximum effectiveness found by Bacot et al. (2022), $Fr_a = 0.93$. For this purpose, optical particle image velocimetry (PIV) measurements were performed for the first time of the detailed flow velocities induced by bubble screens with spargers generating bubbles of different sizes. In addition, high-resolution concentration maps of the lock chamber were made during experiments of the lock-exchange density current across the bubble screens. These measurements were used as a data set for numerical validation of models of bubbly flows (Oldeman et al. 2020).

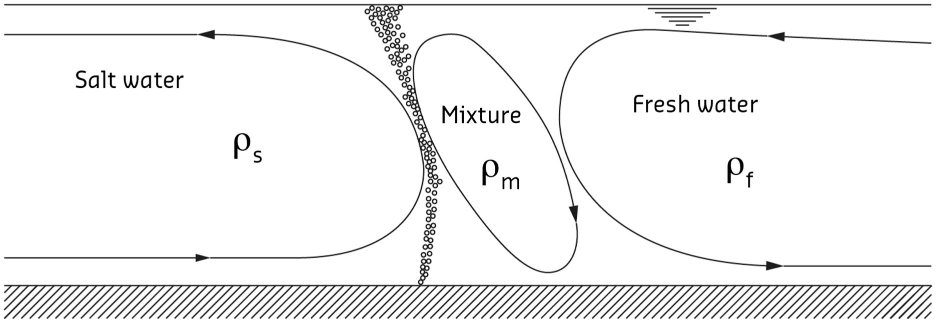

Fig. 2. Flow field elements for a bubble screen between water bodies of differing densities. (Adapted from Abraham et al. 1973.)

Experimental Setup

The flume used for these experiments had a total length of 4.80 m, of which a section of 2.40 m was used and contained using baffles. This section was chosen such that the view of the bubble screen from the side was not hindered by the structural frame comprising the flume, with the sparger being located 0.10 m off-center. The flow section therefore had dimensions of length 2.40 m and width, B, 0.50 m, with a water depth, D, of 0.40 m for all experiments (Fig. 3). The bubble screen sparger was placed in the middle of the flume, splitting the flume into two lock chambers of length, L, 1.20 m, and consisted of two strands, with a small distance between these strands. The width-to-depth ratio B/D in the tests had a value of 1.25, which is small for a lock chamber where this ratio in often in the range of 3–4. It may also be clear that the sparger is relatively large compared with the prototype.

The flume was equipped with a raised floor, approximately 70 mm above the flume's floor, as shown in Fig. 3. The volume under the raised floor was filled, because the exchange of any water across the raised floor would disturb the measurement. The tubes feeding the spargers from the airflow source could then be installed below this false bottom, avoiding any interference with the water flow. The area between the two strands of spargers was not filled with a false bottom, which allowed a well-defined separation by the metal sheet that mimicked the lock door. The metal sheet was thin and had a smooth surface, reducing the effect of lifting it on the flow. The sheet was opened by rapidly lifting it vertically. The coordinate system of the setup was centered at the initial location of the lock gate at the height of the top of the raised floor.

Two types of tests were performed: PIV measurements and concentration measurements (Table 1). The PIV tests provide a detailed flow field that can be compared with the literature, while the

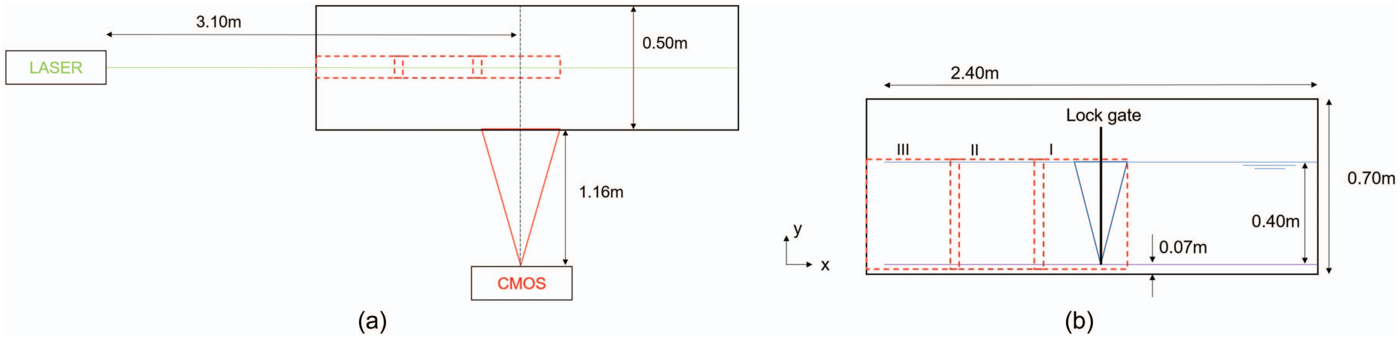

Fig. 3. (Color) Fields of view of the PIV setup within the flume: (a) top view; and (b) side view.

Table 1. Overview of tests performed

Density difference	Bubble size (mm)	Airflow rate Q_a (NL/min)	Froude air number Fr_a	Experiment
$\Delta\rho = 0$ kg/m^3	4–8	33.5	—	PIV, 3 × concentration
		56.0	—	PIV, 3 × concentration
		86.9	—	PIV, 2 × concentration
	1–2	33.5	—	PIV, 2 × concentration
		56.0	—	PIV, 2 × concentration
		86.9	—	PIV, 2 × concentration
$\Delta\rho = 20$ kg/m^3	No bubble screen	—	—	1 × concentration
	4–8	33.5	0.80	2 × concentration
		56.0	0.95	3 × concentration
		86.9	1.10	2 × concentration
	1–2	33.5	0.80	2 × concentration
		56.0	0.95	2 × concentration
		86.9	1.10	2 × concentration

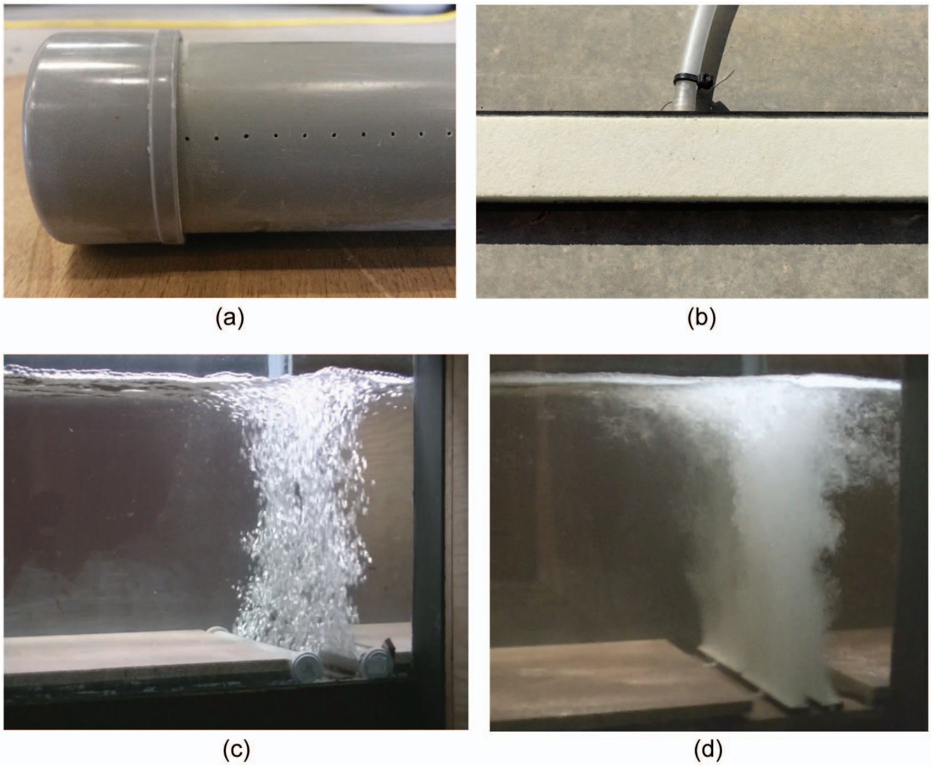

Fig. 4. (Color) Views of the different sparger types: (a) PVC sparger; (b) porous stone sparger; (c) bubble screen from the PVC sparger; and (d) bubble screen from the porous stone sparger.

concentration tests provide the dynamics of the density current in the inhomogeneous tests and the total mixing across the bubble screen. The PIV tests use homogeneous freshwater of density 999 $\mathrm{kg/m^3}$ on both sides of the screen. The concentration measurements were performed both for homogeneous freshwater and for a situation with fluid of different density initially on either side of the screen, with the saltwater side having a density of 1,020 $\mathrm{kg/m^3}$. In these tests, the saltwater was dyed blue. The tests with homogeneous water also had the water in one compartment dyed blue.

Spargers

To create bubble screens with different bubble sizes, two different types of sparger were used. The first type consisted of two PVC pipes of 0.50-m length and 40-mm outer diameter, which were placed on either side of the metal sheet dividing both compartments (Fig. 4). Each PVC pipe was perforated equidistantly with 90 holes of 0.8-mm diameter. The pipes were oriented such that the perforations were located approximately 45° to the vertical, pointing toward each other. The spacing between the two strands was 75 mm. The inflow of air was in the center of both pipes, in the middle of the flume, opposite to the perforations. The PVC pipes were installed such that their top was flush with the false bottom plate. The bubbles generated from this sparger were slightly eccentric in shape and in the wobbling regime in the bubble shape regime map (Clift et al. 1978), the width varying on average between 6.6 and 7.9 mm and the height varying between 4.2 and 4.6 mm (Table 2).

The other sparger type consisted of four porous stone aerators, fixed in two sets of two, with one set on either side of the separating metal sheet (Fig. 4). The upper side of the porous stone was located 17 mm below the upper side of the false bottom plate, which means the outflow of bubbles was approximately 3 mm higher than in the case of PVC pipes. The distance between the two strands was 20 mm. The bubbles from the porous stone aerator were smaller, varying in width from 1.5 to 1.9 mm and in height from 1.3 to 1.6 mm and are thus near the boundary between the spherical regime and the wobbling regime in the bubble shape regime map (Clift et al. 1978).

Table 2. Overview of bubble sizes

Airflow rate	Froude air number		1–2 mm bubbles		4–8 mm bubbles	
Q_a (NL/min)	Fr_a	Dimension	Mean (mm)	SD (mm)	Mean (mm)	SD (mm)
33.5	0.80	Width	1.5	0.6	6.6	1.7
		Height	1.3	0.5	4.2	0.7
56.0	0.95	Width	1.8	0.7	7.8	0.7
		Height	1.5	0.6	4.3	0.9
86.9	1.10	Width	1.9	0.7	7.9	1.4
		Height	1.6	0.6	4.6	0.9

The airflow was measured with two mass flowmeters and controllers (Bronkhorst, Ruurlo, Netherlands), each with a range of 0–50 normal liter (NL)/min. The rated accuracy of this instrument is 1.3% for the lowest tested airflow rate and 0.7% for the highest tested airflow rate.

PIV Measurements

The PIV camera was positioned alongside the flume, looking in the y-direction. Three fields of view (FoVs), as shown in Fig. 3, were measured independently by repeating the same experiment at least three times, moving the camera each time. The FoVs were 0.50×0.40 m, accounting for a slight overlap in adjacent FoVs. All three were on the left side of the bubble screen, assuming symmetry of the flow field.

The flow was imaged using a complementary metal oxide semiconductor (CMOS) sensor with 2,048 × 2,048 pixels (LaVision Imager MX4M, Göttingen, Germany). The distance to the nearest wall of the flume was 1.16 m. The bit depth of the sensor was 10 bit. The pixel size was 5.5 μm. For every flow condition and for all three FoVs, two types of data were recorded: (1) high acquisition frequency of 20 Hz (200 images), showing the real-time behavior of the bubble screen for a short time span; and (2) and reduced acquisition frequency of 1 Hz (1,000 images, i.e., a period of approximately 17 min), providing a statistically independent set of velocity data. The results in this paper are based on the latter, statistically independent data. The tracer particles were illuminated using a dual-cavity Nd:YAG laser (Litron NL 50-100, Warwickshire, England). The maximum output was 50 mJ and the wavelength of the light was 532 nm. The laser was located at the end of the flume, at a distance of 0.80 m from the tank, i.e., 3.10 m from the bubble screen. Fluorescent orange polyethylene microspheres of 90 to 106 μm diameter were used as tracer particles. The densities of these particles were 990 to 1,010 $\mathrm{kg/m^3}$, i.e., practically neutrally buoyant. An optical long-pass filter (cut-on wavelength 590 nm) was mounted on the objective [Nikon (Minato-ku, Tokyo) Micro-Nikkor with focal length of 28 mm], ensuring that only the light reflected from the particles would reach the sensor and the light from the bubbles would not. The peak of the daylight color of the particles was 606 nm.

The PIV interrogation consisted of performing background subtraction followed by one pass on 64 × 64-pixel interrogation areas with 50% overlap followed by two passes on 48 × 48-pixel interrogation areas with 50% overlap. In some cases in Plane 2, the final two passes were performed on a domain size of 32 × 32 pixels with 50% overlap. Varying requirements for the minimum allowable peak ratio were used between 1.2 and 1.5 and universal outlier detection (Westerweel and Scarano 2005) was applied. The target percentage of valid vectors was 95%, except inside the bubble screen. Inside the bubble screen, the regions where more than 550, and in some cases 500, out of the 1,000 vectors were invalid were masked. This was done in order to rely mostly on validated displacement quantifications from tracer particle image displacements. The shape of the masked bubble plume area was observed to resemble the shape of the image area where no clear particle images can be seen due to the air bubbles being present between the illuminated particles and the camera. Due to the dynamic behavior of the plume and the finite paraxial imaging angle, the shape of the masked bubble plume area was not necessarily equal to the mean bubble plume shape. Isolated remaining valid vectors inside the bubble screen area were masked manually.

Concentration Measurements

Similar to the PIV measurements, for the experiments with dye imaging the tank was placed in an optically controlled environment to avoid any effect of changing outside light conditions. The dye concentrations were recalibrated at the start of each test to account for any changes in inside light conditions.

The dye used was blue tracer dye by Cole-Parmer (Vernon Hills, Illinois). The dye was mixed thoroughly before the test, together with brine for the cases with a density difference. A density difference of 20 $\mathrm{kg/m^3}$, or 2%, was used and measured using a conductivity and temperature sensor (Yokogawa SC72, Yokogawa Measurement Corporation, Hachioji-shi, Tokyo). The test sequence was as follows:

1. The tank was filled and the metal sheet put in place to get two compartments that were equally filled.
2. The dye was thoroughly mixed in the right-side compartment, as was the salt (using brine of approximately 1,260 $\mathrm{kg/m^3}$).
3. The density of the right-side compartment was checked.
4. The bubble screen was started and a flow developed in the tank.
5. The separating plate was removed manually to begin the exchange process.

One monochrome camera was used for the concentration measurements (Retiga 1300C, Teledyne QImaging, Surrey, British Columbia, Canada). The acquisition frequency was 10.2 ± 0.3 Hz. The CCD sensor imaged frames of 904 × 664 pixels. The bit depth was 12 bit. The pixel size was 6.7 μm. An objective with a focal length of 35 mm (Fujinon HF35SA-1, Minato-ku, Tokyo) was mounted on the camera. The camera was oriented to be looking at the tank perpendicularly from the side (i.e., in the z-direction), halfway along the tank's length and at a distance of 7.50 m, the maximum distance available in the facility. This led to a maximum viewing angle in the measurement domain of 8.5°, which led to an increase of travel distance of light through the tank of approximately 1% at the sides relative to the center. Behind the tank (thus at the side opposite of the camera), two rectangular LED panels were placed, one at each side of the tank. The back of the tank was covered with white, semitransparent acrylic plates to provide uniform lighting of the tank. Remaining nonuniformity was taken into account by calibration of the postprocessing, treated in the next section. Per measurement, 1,230 images were taken.

The setup also included four conductivity measurement rods, referred to as geleidendheid en concentratie meter (GCM) sensors, with six measurement points along the wetted vertical. Three of these rods were located in the left-side compartment, at 1/8, 1/4, and 3/8 of the flume length, and the fourth rod was located halfway along the right-side compartment (at 3/4 of the flume length) as visible in Fig. 6. A temperature sensor was installed in both compartments. The measured conductivity was converted to salinity via

$$S(T,\sigma)=\left(\frac{\sigma}{2.314\times((8.018\cdot 10^{-3}T+1.0609)^2-0.5911)}\right)^{1/92}$$

Then the density was calculated as $\rho(T,S)=999.904+4.8292\cdot 10^{-2}T-7.2312\cdot 10^{-3}T^2+2.9963\cdot 10^{-5}T^3+0.76427S-3.1490\cdot 10^{-3}ST+3.1273\cdot 10^{-5}ST^2$ (Delft Hydraulics 1981). The measurements of these instruments and the camera recording were synchronized upon opening the gate using an LED visible within the camera's view to provide a cross-check of the calibrated density from the camera postprocessing of the camera images.

Calibration of Concentration Experiments

Using calibration images, one can derive density fields from the images of the measurement. The calibration was obtained by filling both compartments of the tank with a water-dye solution of a known concentration, imaging this, and repeating this for 12 mixtures at different increasing concentrations. The calibration thus resulted in a curve per pixel, relating gray value to concentration (see Fig. 5 for an example result for one pixel). For intermediate gray values, a piecewise linear interpolation was adopted. This method is equal to the calibration method used in Nogueira et al. (2013). The calibration was repeated several times during the test series. The pixels whose values were affected by the presence of bubbles were removed from the analysis, as were those concealed by the frame supports and measurement rods. These pixels were unavailable when calculating the total salt mass on the left side of the flume. The parts of the image that were not used were masked. The bubble screen mask (which also covers the frame) comprises approximately

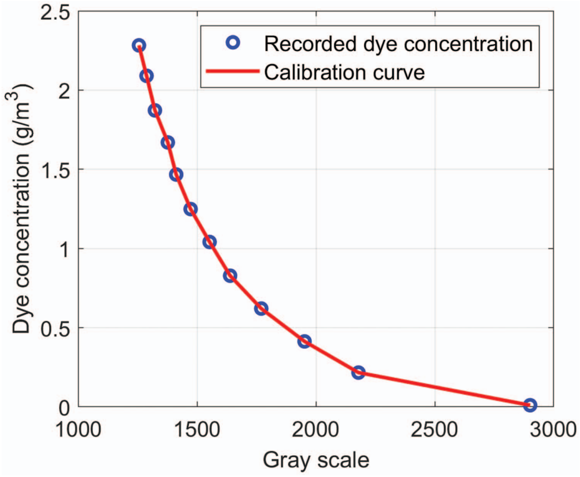

Fig. 5. (Color) Example calibration curve for a single pixel.

10% of the pixels of the image. The masks covering the measurement rods comprise less than 3% of the pixels. An example result is shown in Fig. 6 where the mask for the bubble screen (shown within two thin diagonal lines), the frame, and the rods can be clearly seen. For the total salt mass on the left side of the flume in the case of a porous stones sparger, a moving average of 10 frames was used because of signal noise. This was assumed to be the result of the smaller bubbles in the experiment being suspended in the main recirculation cell but not being removed by the mask.

Experimental Conditions

The overview of the tests is given in Table 1. The PIV experiments were only performed for the homogeneous ($\Delta\rho = 0$) cases. The three airflow rates were chosen such that they were in the range in which bubble screens are used in practice for the mitigation of salt intrusion at locks, namely, $Fr_a \approx 1$. The chosen flow rates were sufficient to investigate the different regimes identified by Bacot et al. (2022), the lower flow rate being in the breakthrough regime, the higher flow rate being in the curtain-driven regime, and the other flow rate being very close to value found by those researchers to have the minimum salt transmission factor. The concentration measurements were each repeated to check the repeatability of the results. Finally, a test of a density current in the flume without a bubble screen was performed to act as a reference for the assessment of the effectiveness of the bubble screen in mitigating mixing from one side of the tank to the other.

Results and Discussions

PIV Results

Velocity Distribution

Fig. 7 shows the velocities induced by the bubble screens, for the case where $Q_a = 86.9$ (NL/min) in homogeneous water. The image shows the three fields of views combined, without interpolation. The color denotes the velocity magnitude, and the arrows show the magnitude as well as the direction. One in every four vectors is shown. The scaling of the vectors differs per field of view. The gray rectangular area near $x = -1{,}100$ mm is due to a structural beam blocking optical access. The dark blue area at the bubble screen location is the mask based on the number of valid vectors. Near the water surface and in the bubble screen itself no values are presented because it is expected that the PIV is not accurate in these areas owing to reflections of light from the surface and bubbles. Away from the screen a clear recirculation zone is shown,

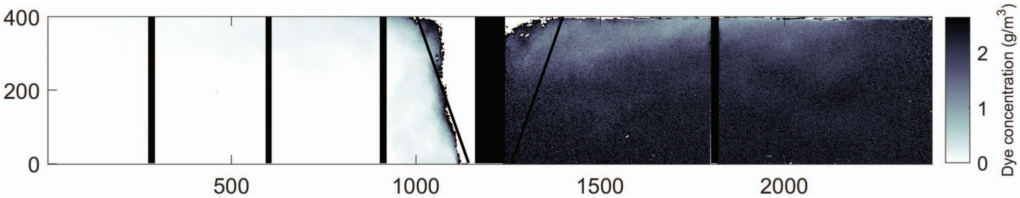

Fig. 6. (Color) The mask used in obtaining the total mass of salt on the left side, such as to avoid the hindrance of the bubble screen and frame in the postprocessing. The axes give the position in millimeters.

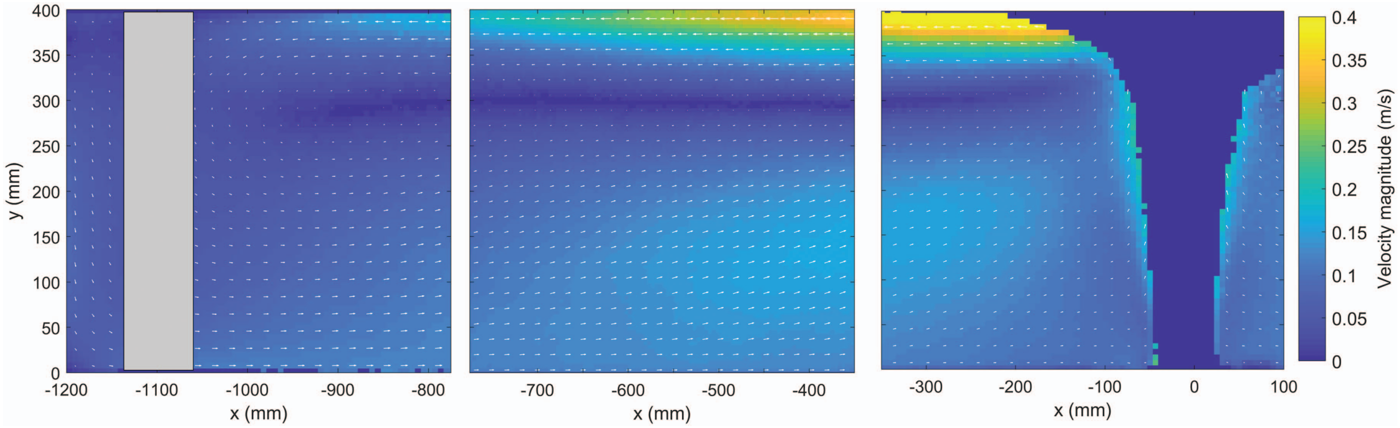

Fig. 7. (Color) Flow velocities measured on the left side of the tank, measured with PIV for case with 4–8 mm bubbles for $Q_a = 86.9$ NL/min. Color denotes the flow velocity magnitude (m/s).

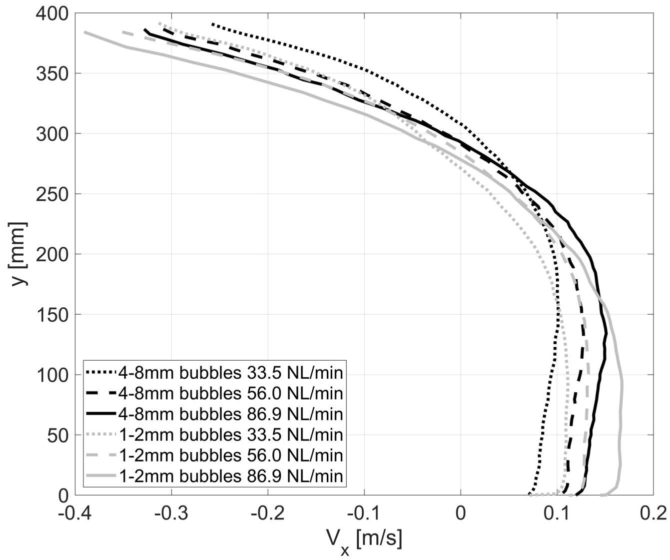

Fig. 8. Vertical profiles of the flow velocities for various airflow rates and bubble sizes; taken from the PIV measurements at $x = -D$.

with highest flow velocities near the surface. The lower layer, flowing toward the bubble screen, covers approximately $3/4$ of the water depth. Velocities at verticals far from the screen (e.g., at $x = -900$ mm) are mostly horizontal, with a negligible vertical component. Closer to the screen, roughly from $x = -600$ mm to $x = -100$ mm, the horizontal and upward component are nearly equal, giving a flow direction between 30° to 45° upward. The flow field in general shows qualitative agreement with flow fields shown in literature (Riess and Fanneløp 1998) with the recirculation zone equal in size to the available half of the tank.

Velocity Profiles

The quantitative comparison of the vertical velocity profiles of horizontal velocity for different bubble sizes and airflow rate is given in Fig. 8 at a distance $x = -D$, on the left side of the screen. The results show a profile shape in accordance with previous literature where a surface current away from the screen is present in the upper portion of the water column. In the lower portion of the water column the flow is directed toward the bubble screen because part of this water is entrained with the upward-flowing bubble jet. A higher airflow rate leads to greater magnitudes of velocity at the surface. The bubble screen with smaller bubbles induces higher flow velocities at the flume floor and the water surface. The figure shows that the flow velocities at the surface induced by the small bubbles for the medium airflow rate are similar to those resulting from the large bubbles at the highest airflow rate, which indicates that using a smaller bubble size can result in a reduction in the required flow rate for a given induced surface current. The location at which the surface current begins is seen to vary between approximately $y =$ 270 and 305 mm, giving a surface current height of $0.24D$–$0.32D$, which is in the same range as previous experiments but shows a much greater variation than previously seen. Clearly the bubble screen with the small bubbles size gives a larger surface current height, which suggests the large variation is caused by the difference in bubble size. The combination of larger surface velocities and larger current height for the screen with the smaller bubbles could be attributed to increased entrainment in plumes with smaller bubbles as has been shown in earlier studies (Neto et al. 2008).

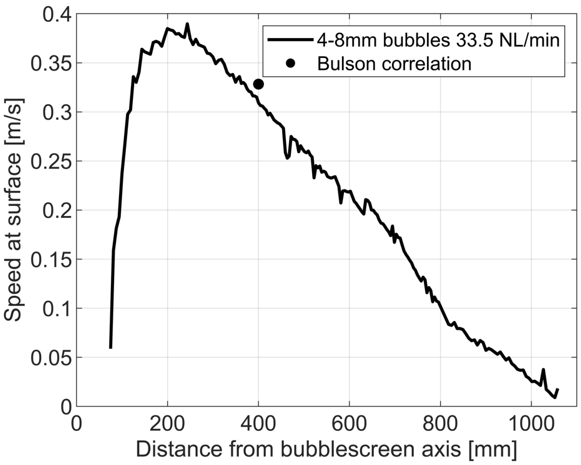

Fig. 9. Estimated speed at the surface as a function of distance from the bubble screen, extrapolated from the PIV velocity profiles. Case with 4–8 mm bubbles with flow rate 33.5 NL/min.

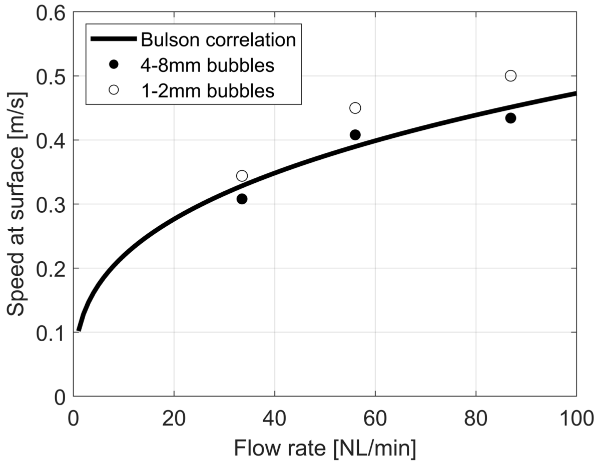

Fig. 10. Comparison of the estimated surface velocities at $x/D = 1$ for the experiments with the correlation of Bulson [Eq. (1)].

Surface Velocity

Although the PIV results near the surface are not reliable, they can be extrapolated from the velocities near the surface. This is comparable with how the surface velocities were inferred in earlier experimental studies in the literature (Bulson 1961; Wen and Torrest 1987). This has been done for all PIV experiments and an example is given in Fig. 9 for the case of small bubbles with a flow rate of 33.5 NL/min. The extrapolation was done by taking the average gradient of the measurements nearest the surface. The decay of velocity away from the bubble screen seems to follow a linear profile after reaching a maximum at a little more than $0.5D$ from the axis. The literature suggests a decay proportional to $x^{-1/2}$ for a wall jet (Rajaratnam 1976). The measurements of Bulson (1961) and Wen and Torrest (1987) also show this. That the profile in the current experiments is linear suggests that the tank is not long enough for the wall jet to develop unhindered by the end wall of the tank. This relation is repeated in all experiments. A comparison was made (Fig. 10) with the correlation of Bulson [Eq. (1)] for the surface velocities at $x = D$ for all tests. The relation of the surface velocity as a function of the flow rate is well captured. This shows that the limitation of the short tank does not greatly affect the flow field

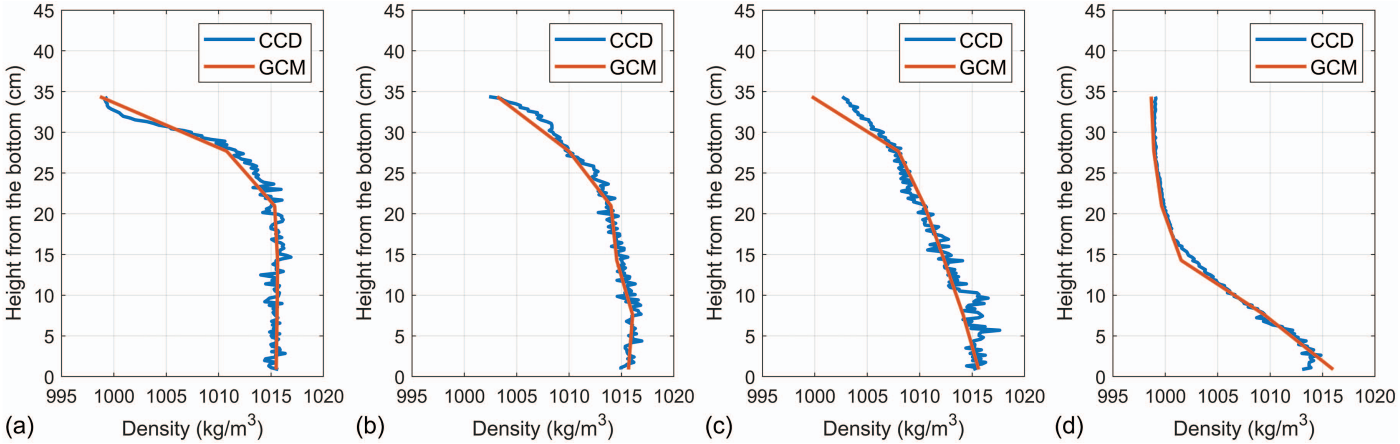

Fig. 11. (Color) Vertical profiles of the density at four locations in the tank during unhindered lock-exchange experiment, comparing the profiles taken from the optical measurement technique (CCD) with the measurement rods (GCM): (a–c) left side of the tank; and (d) right side of the tank.

generated close to the bubble screen $x \leq D$ even if the decay of the surface current beyond this point may be influenced by the short tank. The current setup is therefore sufficient for drawing conclusions about the initial intrusion of salt through the bubble screen but not the size of the recirculation cell nor the transport of salt farther from the screen or at times after the initial phase.

Concentration Measurement Results

Density Profiles

Fig. 11 shows the density at four verticals in the tank: Figs. 11(a–c) are in the left-side compartment and Fig. 11(d) in the middle of the right-side compartment. The conductivity measurement instruments (GCM) had six measurement points in the vertical. To compare these with the results of the concentration recording (CCD), the density according to the latter was taken from the salt concentration maps at this coordinate. A spatial average over the immediate neighboring pixels was taken. The profile from the concentration measurements shows some noise because no filtering was used. However, the agreement between the optical measurement technique and the measurement rods instruments was good. The GCM measurements volume was very limited and near the gauge, whereas the density derived from the optical technique was in fact a width-averaged density. The agreement between the two measurements suggests that the flow was quite 2D without large variations in the width. The density from the concentration measurements allows a higher spatial resolution in the vertical, which better defines the density current. An obvious added value of this measurement technique is that the complete data in fact are a two-dimensional spatial map, i.e., not limited to these four verticals, and therefore allow a more complete interpretation of the current. Furthermore, it is a nonintrusive measurement technique.

Concentration Fields

The concentration fields, $c(x, y; t)$, for the dye were extracted at each time. This gives very detailed spatial information on the development of the density current and concentration field in each case. Fig. 12 shows an instantaneous concentration field at 10 s for a case with a density difference of $\Delta\rho = 20\ \mathrm{kg/m^3}$ for different flow rates for the case of large bubbles. The denser fluid is visible on the right side. The bubble screen is pushed to the left due to the higher local pressure in the denser fluid. For the low flow rate, leakage of saltwater is visible both at the top and at the bottom of the tank. The leakage at the bottom is more pronounced. This is consistent with the concentration and density fields found in Bacot et al. (2022) for the breakthrough regime. For the higher flow rates, the leakage at the top of the tank is stronger. This suggests that for the lower flow rate the density current is still strong enough to penetrate partially through the screen. For the highest flow rate all leakage can be attributed to the upward entrained flow in the screen, the so-called curtain-driven regime (Bacot et al. 2022). The most separation of the salt and freshwater bodies may therefore be achieved with a flow rate for which the density current along the bottom is just fully hindered. After that point more airflow simply induces more

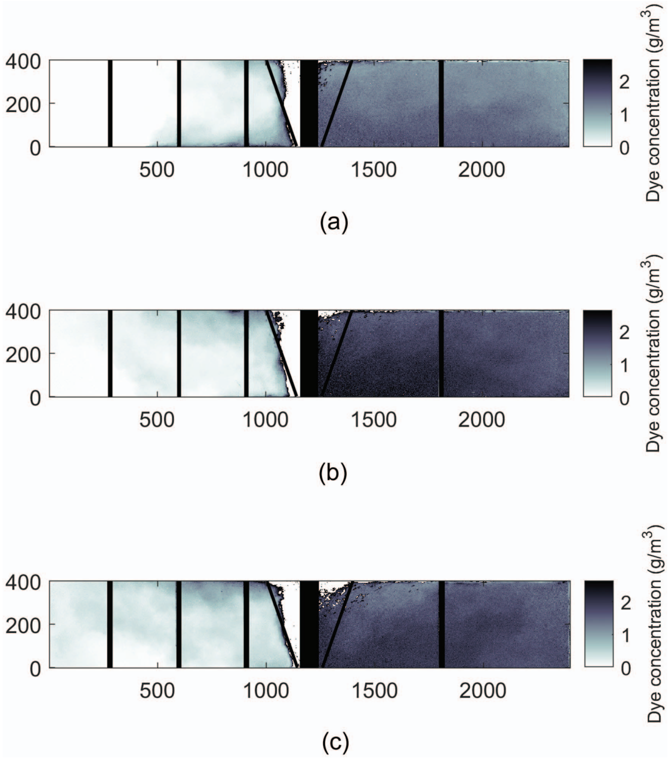

Fig. 12. (Color) Concentration fields at 10 s for $\Delta\rho = 20\ \mathrm{kg/m^3}$ and the case of large bubbles at different airflow rates: (a) $Fr_a = 0.80$; (b) $Fr_a = 0.95$; and (c) $Fr_a = 1.10$. The axes show position in millimeters.

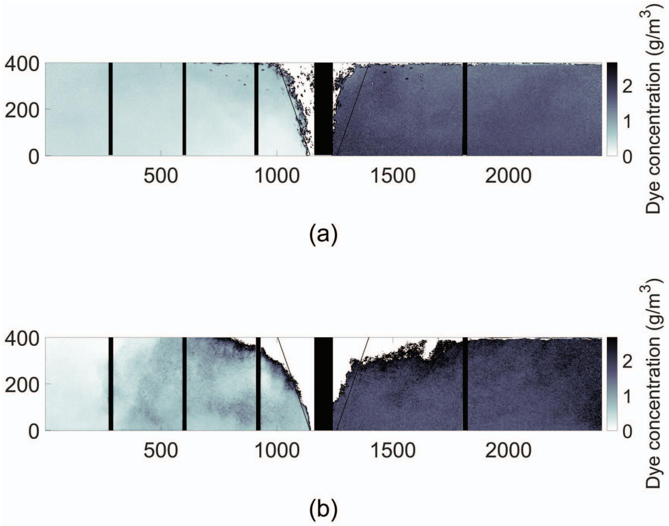

Fig. 13. (Color) Concentration fields at 18 s for $\Delta\rho = 20\ \mathrm{kg/m^3}$ and the flow rate $Fr_a = 0.95$ for the cases of (a) large bubbles; and (b) small bubbles. The axes show position in millimeters.

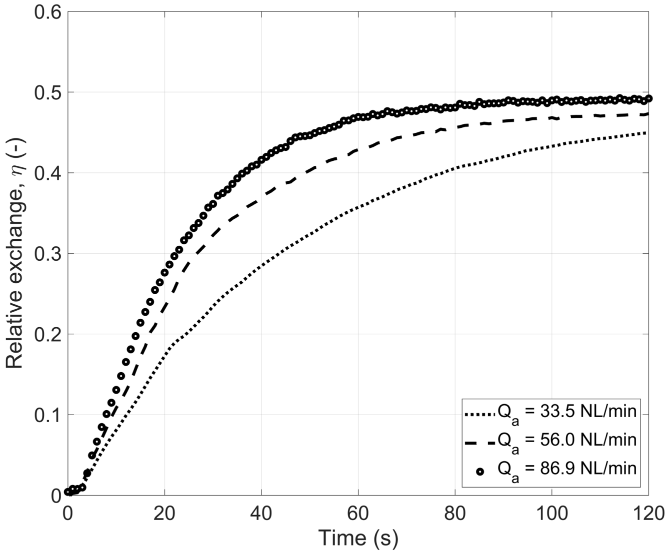

Fig. 14. Relative exchange as a function of time for different airflow rates in a $\Delta\rho = 0\ \mathrm{kg/m^3}$ situation for 4–8 mm bubbles.

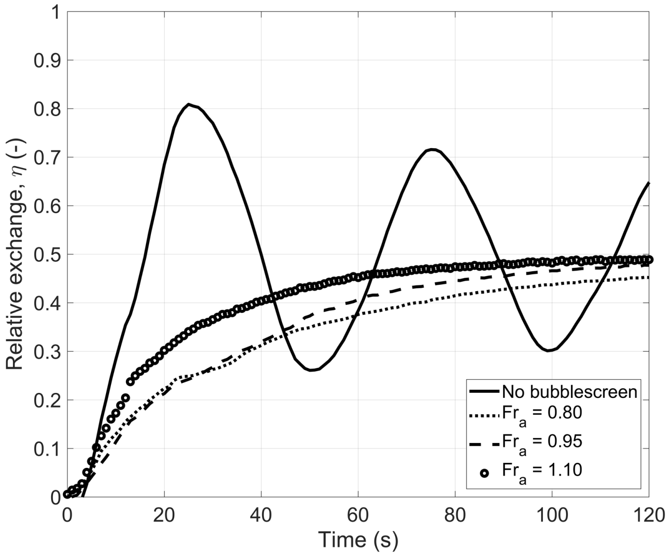

Fig. 15. Relative exchange as a function of time for different airflow rates in a $\Delta\rho = 20\ \mathrm{kg/m^3}$ situation for 4–8 mm bubbles.

mixing from one side to the other. The middle flow rate, $Fr_a = 0.95$, is consistent for the large bubble case with the point of transition between the breakthrough regime and curtain-driven regime (Bacot et al. 2022). The concentration field shown in Fig. 12 for this flow rate indeed shows a suppression of the density current along the bottom of the tank but no strong leakage along the surface.

Fig. 13 shows a comparison of density fields at 18 s for the same flow rate, $Fr_a = 0.95$, but for different bubbles sizes. At this moment, 18 s, the leakage of salt through the screen with larger bubbles is equally distributed over the height of the tank, with no obvious dominance of leakage through surface current or density current along the floor. For the small bubble case the leakage through the surface current is clearly dominating, which suggests that this screen is in the curtain-driven regime. It can be concluded, therefore, that the point of transition between the regimes (and the airflow rate for which maximum effectiveness is achieved) is dependent on the bubble size.

Relative Exchange

We define a relative exchange, η, as the ratio of the total volume of dye on the left side of the tank (initially zero) to the total volume of dye in the whole tank

$$\eta(t) = \frac{\int_0^D \int_{-L}^0 c(x,y;t)dxdy}{\int_0^D \int_{-L}^L c(x,y;0)dxdy} \qquad (3)$$

Fig. 14 shows the total amount of dye in the left-hand compartment of the tank for the screen with large bubbles at the three tested airflow rates, in homogeneous water, against time. Initially the tank is unmixed and eventually all tests tend to a mixture of 50%. The exchange increases with the increasing airflow rate. At $t = 40$ s, for instance, the dye percentages at the left side are 28%, 38%, and 42% for flow rates of 33.5, 56.0, and 86.9 NL/min, respectively. Because there is no density current in the homogeneous situation, the exchange is solely the action of the induced advection currents from the bubble screen.

When an initial density difference is present across the dividing plate, a density current will be responsible for part of the exchange of dye from one side to the other. Without a bubble screen the exchange is fast (Figs. 15 and 16). The first 5 s are affected by the removal of the dividing plate and the unhindered lock exchange is initiated only after this time. The sloshing of the density current is evident from the sinusoidal-type signal. After the density current reflects from the end wall of the tank, the left side can almost fill up with the dye (>80%), while the right side would be nearly empty of dye. Fig. 15 shows the performance of the screen with larger bubbles for different airflow rates (expressed here as a Froude air number). This density current is clearly hindered by the presence of the bubble screen. Initially ($t < 20$ s) the two lower flow rates perform comparably, and better than the higher flow rate. Later ($t > 20$ s) the behavior is more similar to the homogeneous case, indicating that eventually the bubble screen acts as a mixer, with a higher flow rate providing more and faster exchange. Only the case of flow rate 56.0 NL/min ($Fr_a = 0.95$) is able to reduce the exchange of dye compared with the situation where no density difference was present (see again at $t = 40$ s where for that flow rate the exchange is 33% compared with 38% from the homogeneous case).

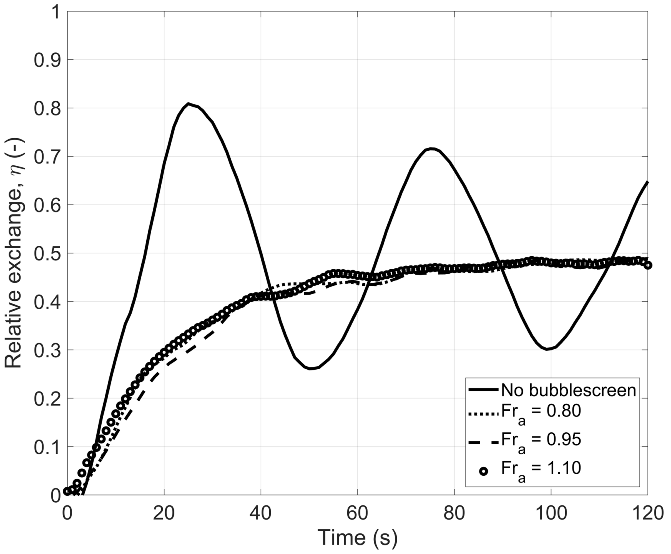

Fig. 16. Relative exchange as a function of time for different airflow rates in a $\Delta\rho = 20\ \mathrm{kg/m^3}$ situation for 1–2 mm bubbles.

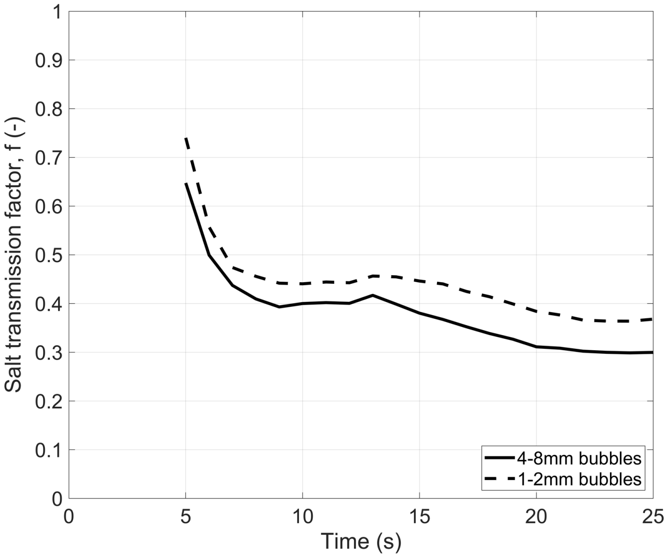

Fig. 17. Salt transmission factor of the bubble screen in time for both sparger types for the flow rate $Fr_a = 0.95$.

The screen with small bubbles shows much less difference between the flow rates (Fig. 16). Here the results are very similar to each other and the case with the screen of larger bubbles for a higher flow rate. Only in the first 10 s of the test is there a noticeable difference in performance. This can be attributed to the smaller bubbles being able to entrain more fluid from the surroundings, making this type of screen a more effective mixer. This may help the bubble screen be more effective at low flow rates $Fr_a < 0.8$, but for the flow rates tested in this study an increase in flow rate is not leading to better separation.

Bubble Screen Effectiveness

We define a salt transmission factor, f, as the ratio of the relative exchange for a scenario as a proportion of the relative exchange of an unprotected lock, η_0

$$f = \frac{\eta(t)}{\eta_0(t)} \tag{4}$$

Fig. 17 shows the effectiveness of the bubble screen over time for the airflow rate corresponding to $Fr_a = 0.95$. Here we see the development over time, which gives a better indication of how the moment the gate in a lock is closed would influence the relative exchange. The effect of the bubble size is visible. Although the two bubble screens perform to a similar degree in the early seconds, it is clear that the screen with larger bubbles performs better overall. A similar result is seen for $Fr_a = 0.8$ (Figs. 15 and 16) but not for $Fr_a = 1.1$, where the performance of the two bubble screens is almost identical. It can be hypothesized that the screen with smaller bubbles creates more mixing within the screen and subsequently more saltwater is ejected onto the freshwater side at the surface. This cannot be verified with the results of these experiments because they do not give information of the dye concentration within the screen. This, however, has been studied via numerical simulations in Oldeman et al. (2020).

Conclusions

Experiments were performed of a laboratory-scale bubble screen with high-resolution optical techniques. Experiments were made for bubble screens for three different airflow rates with two different spargers, leading to screens of different bubble sizes. The amount of dye exchanged across the screen after the release of a lock gate at the screen was measured in the homogeneous case (fluid of the same density on either side) and the inhomogeneous case (fluids of different density on either side). The inhomogeneous case is representative of the application of bubble screens as a salt intrusion mitigation measure at shipping locks.

Previous studies have only made low-resolution flow measurements of the bubble screen–induced flow field. In this paper, detailed flow patterns for the homogeneous situation in the entire circulation cell on one side of the screen were made, although the size of the cell was limited in this case by the tank size. Additionally, the effect of bubble size was shown for the first time with smaller bubbles inducing larger surface velocities. In the homogeneous case, a higher flow rate led to faster mixing of dye across the screen after release of the lock gate.

For the inhomogeneous case, the screen acted as a separator of the fluids of different densities after release of the lock gate, delaying the exchange of dye relative to the case without a bubble screen. The detailed concentration fields produced here show different flow regimes in the inhomogeneous situations as described elsewhere in the recent literature (Bacot et al. 2022). A breakthrough regime at low flow rates is characterized by a density current along the bottom of the tank because the bubble screen is not strong enough to arrest the lock-exchange flow. A curtain-driven regime has exchange driven by the upward-entrained fluid inside the screen, which is ejected outward at the top of the tank. For the case with relatively large bubbles (4–8 mm) these exchange mechanisms appeared in balance for $Fr_a = 0.95$. This is in line with earlier results in the literature, which suggest a change of regime for $Fr_a = 0.93$.

However, this paper also showed for the first time the impact of bubble size on the effectiveness of the bubble screen as a separator of fluids of different densities. For the bubble screen with smaller bubbles, the curtain-driven regime was found to be initiated at lower flow rates with the test with $Fr_a = 0.95$ clearly in that regime. In addition, for the flow rates tested in this paper, the screen with larger bubbles performed better as a separator. Finding how the optimum airflow rate changes for bubble screens of different bubble sizes should be a subject of future research and would help inform bubble screen design in practice for use as a salt intrusion mitigation measure at locks.

Data Availability Statement

All data, models, or code that support the findings of this study are available from the corresponding author upon reasonable request.

Acknowledgments

The authors wish to acknowledge the help of several students and colleagues in the preparation, execution, and analysis of this experiments: Babette Haitsma Mulier, Bart Veenings, Gijs Verbeeten, Gijs Wolbert, Pam van Zaanen, Lina Nikolaidou, and Jesil Kurian. We thank Helena Nogueira for careful reading and helpful comments on the drafts of the paper. In particular, the authors would like to thank Arthur Oldeman and colleagues from the Technical University of Eindhoven for their assistance in processing the data and discussions. This work was conducted with Topconsortium voor Kennis en Innovatie (TKI) funding from the Dutch Ministry of Economic Affairs (Grant #2017DEL002).

Notation

The following symbols are used in this paper:

c = dye concentration;
D = water depth (m);
Fr_a = Froude air number;
g = gravitational acceleration ($\mathrm{m/s^2}$);
g' = reduced gravity, $\Delta\rho/\rho$, ($\mathrm{m/s^2}$);
H_0 = atmospheric pressure in length column of water (m);
L = lock length (m);
Q_a = airflow rate through sparger, normalized to atmospheric pressure (NL/min);
q = airflow rate per unit width ($\mathrm{m/s^2}$);
t = time (s);
V_m = surface velocity (m/s);
V_x = horizontal velocity (m/s);
x, y, z = Cartesian coordinates, with origin at the base of the tank at the location of the screen (m, m, m);
δ = surface current height (m);
η = relative exchange of dye; and
ρ = density ($\mathrm{kg/m^3}$).

References

Abraham, G., and P. van der Burgh. 1964. "Pneumatic reduction of salt intrusion through locks." *J. Hydraul. Div.* 90 (1): 83–119. https://doi.org/10.1061/JYCEAJ.0001009.

Abraham, G., P. van der Burgh, and P. de Vos. 1973. *Pneumatic barriers to reduce salt intrusion through locks*. The Hague, Netherlands: Rijkswaterstaat Communications.

Bacot, A., D. Frank, and P. F. Linden. 2022. "Bubble curtains used as barriers across horizontal density stratifications." *J. Fluid Mech.* 941 (1): A1. https://doi.org/10.1017/jfm.2022.142.

Benjamin, T. B. 1968. "Gravity currents and related phenomena." *J. Fluid Mech.* 31 (2): 209–248. https://doi.org/10.1017/S0022112068000133.

Blanckaert, K., F. A. Buschman, R. Schielen, and J. H. Wijbrenga. 2008. "Redistribution of velocity and bed-shear stress in straight and curved open channels by means of a bubble screen: Laboratory experiments." *J. Hydraul. Eng.* 134 (2): 184–195. https://doi.org/10.1061/(ASCE)0733-9429(2008)134:2(184).

Bulson, P. S. 1961. "Currents produced by an air curtain in deep water." *Dock Harbour Authority* 42 (487): 15–22.

Clift, R., J. R. Grace, and M. E. Weber. 1978. *Bubbles, drops and particles*. Cambridge, MA: Academic Press.

Dai, A., and Y. L. Huang. 2020. "Experiments on gravity currents propagating on unbounded uniform slopes." *Environ. Fluid Mech.* 20 (6): 1637–1662. https://doi.org/10.1007/s10652-020-09758-2.

De Falco, M. C., L. Ottolenghi, and C. Adduce. 2020. "Dynamics of gravity currents flowing up a slope and implications of entrainment." *J. Hydraul. Eng.* 146 (4): 04020011. https://doi.org/10.1061/(ASCE)HY.1943-7900.0001709.

Delft Hydraulics. 1981. *New accurate density formulations for pure water and saline solution: Density as a function of temperature and salt concentrations*. [In Dutch.] Rep. No. S205-1. Delft, Netherlands: Delft Hydraulics.

Dugué, V., K. Blanckaert, Q. Chen, and A. J. Schleiss. 2015. "Influencing flow patterns and bed morphology in open channels and rivers by means of an air-bubble screen." *J. Hydraul. Eng.* 141 (2): 04014070. https://doi.org/10.1061/(ASCE)HY.1943-7900.0000946.

Evans, J. T. 1955. "Pneumatic and similar breakwaters." *Proc. R. Soc. London, Ser. A* 231 (1187): 457–465. https://doi.org/10.1098/rspa.1955.0187.

Fanneløp, T. K., S. Hirschberg, and J. Küffer. 1991. "Surface current and recirculating cells generated by bubble curtains and jets." *J. Fluid Mech.* 229 (Aug): 629–657. https://doi.org/10.1017/S0022112091003208.

Inghilesi, R., C. Adduce, V. Lombardi, F. Roman, and V. Armenio. 2020. "Axisymmetric three-dimensional gravity currents generated by lock exchange." *J. Fluid Mech.* 851 (Sep): 507–544. https://doi.org/10.1017/jfm.2018.500.

Keetels, G., R. Uitteenbogaard, J. Cornelisse, N. Villars, and H. van Pagee. 2011. "Field study and supporting analysis of air curtains and other measures to reduce salinity transport through shipping locks." *Irrig. Drain.* 60 (1): 42–50. https://doi.org/10.1002/ird.679.

Kerstma, J., P. A. Kolkman, H. J. Regeling, and W. A. Venis. 1994. *Water quality control at ship locks*. Rotterdam, Netherlands: A. A. Balkema.

Kobus, H. E. 1968. "Analysis of the flow induced by air-bubble systems." In *Proc., 11th Conf. on Coastal Engineering*. Reston, VA: ASCE. https://doi.org/10.1061/9780872620131.

Lima Neto, I. E., D. Z. Zhu, and N. Rajaratanam. 2008. "Effect of tank size and geometry on the flow induced by circular bubble plumes and water jets." *J. Hydraul. Eng.* 134 (6): 833–842. https://doi.org/10.1061/(ASCE)0733-9429(2008)134:6(833).

Lombardi, V., C. Adduce, and M. La Rocca. 2018. "Unconfined lock-exchange gravity currents with variable lock width: Laboratory experiments and shallow-water simulations." *J. Hydraul. Res.* 56 (3): 399–411. https://doi.org/10.1080/00221686.2017.1372817.

Maggi, M. R., C. Adduce, and G. F. Lane-Serff. 2023. "Gravity current interacting with slopes and overhangs." *Adv. Water Resour.* 171 (Jan): 104339. https://doi.org/10.1016/j.advwatres.2022.104339.

Marino, B. M., L. P. Thomas, and P. F. Linden. 2005. "The front condition for gravity currents." *J. Fluid Mech.* 536 (Aug): 49–78. https://doi.org/10.1017/S0022112005004933.

Martin, J. E., and M. H. García. 2009. "Combined PIV/PLIF measurements of a steady density current front." *Exp. Fluids* 46 (2): 265–276. https://doi.org/10.1007/s00348-008-0556-7.

Nakai, M., and M. Arita. 2002. "An experimental study on prevention of saline wedge intrusion by an air curtain in rivers." *J. Hydraul. Res.* 40 (3): 333–339. https://doi.org/10.1080/00221680209499947.

Neto, I. E., D. Z. Zhu, and N. Rajaratanam. 2008. "Air injection in water with different nozzles." *J. Environ. Eng.* 134 (4): 283–294. https://doi.org/10.1061/(ASCE)0733-9372(2008)134:4(283).

Nogueira, H. I. S., C. Adduce, E. Alves, and M. J. Franca. 2013. "Image analysis technique applied to lock-exchange gravity currents." *Meas. Sci. Technol.* 24 (4): 047001. https://doi.org/10.1088/0957-0233/24/4/047001.

Nogueira, H. I. S., C. Adduce, E. Alves, and M. J. Franca. 2014. “Dynamics of the head of gravity currents.” *Environ. Fluid Mech.* 14 (Apr): 519–540. https://doi.org/10.1007/s10652-013-9315-2.

Nogueira, H. I. S., P. van der Ven, T. O’Mahoney, A. De Loor, A. van der Hout, and W. Kortlever. 2018. “Effect of density difference on the forces acting on a moored vessel while operating navigation locks.” *J. Hydraul. Eng.* 144 (6): 04018021. https://doi.org/10.1061/(ASCE)HY.1943-7900.0001445.

Oldeman, A., S. Kamath, M. Masterov, T. O’Mahoney, G. van Heijst, J. Kuipers, and K. Buist. 2020. “Numerical study of bubble screens for mitigating salt intrusion in sea locks.” *Int. J. Multiphase Flows* 129 (Aug): 113321. https://doi.org/10.1016/j.ijmultiphaseflow.2020.103321.

Pérez-Díaz, B., P. Palomar, S. Casanedo, and A. Álvarez. 2018. “PIV-PLIF characterization of nonconfined saline density currents under different flow conditions.” *J. Hydraul. Eng.* 144 (9): 04018063. https://doi.org/10.1061/(ASCE)HY.1943-7900.0001511.

Rajaratnam, N. 1976. *Turbulent jets*. Amsterdam, Netherlands: Elsevier.

Riess, I. R., and T. K. Fanneløp. 1998. “Recirculating flow generated by line-source bubble plumes.” *J. Hydraul. Eng.* 124 (9): 932–940. https://doi.org/10.1061/(ASCE)0733-9429(1998)124:9(932).

Rottman, J. W., and J. E. Simpson. 1983. “Gravity currents produced by instantaneous releases of heavy fluids in a rectangular channel.” *J. Fluid Mech.* 135 (Oct): 95–110. https://doi.org/10.1017/S0022112083002979.

Shin, J. O., S. B. Dalziel, and P. F. Linden. 2002. “Gravity currents produced by lock exchange.” *J. Fluid Mech.* 521 (Dec): 1–34. https://doi.org/10.1017/S002211200400165X.

Simpson, J. E. 1997. *Gravity currents: In the environment and the laboratory.* 2nd ed. New York: Cambridge University Press.

Taylor, G. I. 1955. “The action of a surface current, used as a breakwater.” *Proc. R. Soc. London, Ser. A* 231 (1187): 466–478. https://doi.org/10.1098/rspa.1955.0188.

Uittenbogaard, R. J. C., and K. O’Hara. 2015. “Water–air bubble screens reducing salt intrusion through shipping locks.” In *Proc., 36th IAHR World Congress*. The Hague, Netherlands: International Association for Hydro-Environment Engineering and Research.

van der Kuur, P. 1986. “Locks with devices to reduce salt intrusion.” *J. Waterw. Port Coastal Ocean Eng.* 111 (6): 1009–1021. https://doi.org/10.1061/(ASCE)0733-950X(1985)111:6(1009).

Wang, B., C. C. K. Lai, and S. A. Socolofsky. 2019. “Mean velocity, spreading and entrainment characteristics of weak bubble plumes in unstratified and stationary water.” *J. Fluid Mech.* 874 (Sep): 102–130. https://doi.org/10.1017/jfm.2019.461.

Weiler, O., A. J. van der Kerk, and K. J. Meeuse. 2015. “Preventing salt intrusion through shipping locks: Recent innovations and results from a pilot setup.” In *Proc., 36th IAHR World Congress*. The Hague, Netherlands: International Association for Hydro-Environment Engineering and Research.

Wen, J., and R. S. Torrest. 1987. “Aeration-induced circulation from line sources. I: Channel flows.” *J. Environ. Eng.* 113 (1): 82–98. https://doi.org/10.1061/(ASCE)0733-9372(1987)113:1(82).

Westerweel, J., and F. Scarano. 2005. “Universal outlier detection for PIV data.” *Exp. Fluids* 39 (6): 1096–1100. https://doi.org/10.1007/s00348-005-0016-6.